experiments (8, 9). The Agung data are also consistent with laboratory experiments because the $\Delta^{33}S$ versus $\delta^{34}S$ Agung slope (Fig. 2) is the same as that of the Xe lamp experiment obtained for $\lambda > 220$ nm and very close to that of the KrF laser experiments conducted at 248 nm (8, 9).

The sulfur isotopic anomalies in volcanic samples are much smaller than those observed in Archean rocks older than 2.45 billion years (5, 6, 23, 24). In today's atmosphere, OH radicals remain the main sink of SO_2 emitted after a volcanic eruption, and the $SO_2^* + SO_2$ reaction is a minor reaction when compared to the $SO_2 + OH$ reaction. The sulfur MIF measured in volcanic sulfate recorded in snow is a diluted signal and may actually reach the extreme values recorded in Archean rocks. To estimate the upper limit of the sulfur isotopic anomaly generated by the photooxidation process, researchers should compare the kinetics of the $SO_2 + OH$ and $SO_2^* + SO_2$ reactions. Unfortunately, the rate of $SO_2^* + SO_2$ is controversial (25) and is needed for such quantification.

Sulfur mass-independent composition of volcanic sulfate is a time-dependent process, first displaying a positive $\Delta^{33}S$ followed by a negative $\Delta^{33}S$ at the end of the volcanic plume depositional process. This process occurs on a monthly time scale before SO_2 is fully oxidized in H_2SO_4, indicating a rapid process. The nonzero average $\Delta^{33}S$ observed for the full duration of the event requires two conditions: First, the process creates two reservoirs of MIF with opposing signs; second, these two reservoirs must be physically separated in space and time in addition to having a difference in depositional rates. The only way to explain the oscillation of the $\Delta^{33}S$ sign is to consider the fundamental role of aerosols and sedimentation in preserving the isotopic signal. Microphysical processes must be taken into account in models to reproduce sulfur MIF of stratospheric volcanic sulfate. When the relationship between aerosols and sulfur MIF is established, volcanic plume transport may be understood, allowing a precise glaciological record of the climatic impact of stratospheric eruptions.

References and Notes

1. G. Zielinski, *Quat. Sci. Rev.* **19**, 417 (2000), and references therein.
2. S. Bekki, J. A. Pyle, *J. Geophys. Res.* **99**, 1BB61 (1994).
3. G. J. S. Bluth, C. C. Schnetzler, A. J. Krueger, L. S. Walter, *Nature* **366**, 327 (1993).
4. The deviation from the mass-dependent relationships is calculated by the following equations: $\Delta^{33}S = \delta^{33}S - 1000*[(1 + \delta^{34}S/1000)^{0.515} - 1]$ and $\Delta^{36}S = \delta^{36}S - 1000*[(1 + \delta^{34}S/1000)^{1.91} - 1]$. Considering the small size of the samples, our analytical accuracy, with a 2σ uncertainty, is equal to 0.12‰ for $\Delta^{33}S$ and varies from 0.64 to 1.63‰ for $\Delta^{36}S$. Only $|\Delta^{33}S| > 0.12‰$ and $|\Delta^{36}S| > 0.64‰$ are considered as diagnostic of MIF in the present study. Uncertainties (2σ) are 0.07, 0.19, and 0.53 to 1.59‰ for $\delta^{33}S$, $\delta^{34}S$, and $\delta^{36}S$, respectively.
5. J. Farquhar, H. Bao, M. H. Thiemens, *Science* **289**, 756 (2000).
6. J. Farquhar, B. A. Wing, *Earth Planet. Sci. Lett.* **213**, 1 (2003).
7. A. A. Pavlov, J. F. Kasting, *Astrobialogy* **2**, 27 (2002).
8. J. Farquhar, J. Savarino, S. Airieau, M. H. Thiemens, *J. Geophys. Res.* **106**, 32B29 (2001).
9. J. Farquhar, J. Savarino, T. L. Jackson, M. H. Thiemens, *Nature* **404**, 50 (2000).
10. H. Ohmoto, Y. Watanabe, H. Ikemi, S. R. Poulson, B. E. Taylor, *Nature* **442**, 90B (2006).
11. A. Romero, M. H. Thiemens, *J. Geophys. Res.* **108**, 10.1029/2003JD003660 (2003).
12. J. Savarino, A. Romero, J. Cole-Dai, S. Bekki, M. H. Thiemens, *Geophys. Res. Lett.* **30**, 10.1029/2003GL01B134 (2003).
13. S. D. Doiron, Z. Scott, G. J. S. Bluth, C. C. Schnetzler, A. J. Krueger, *EOS Trans. Am. Geophys. Unian* **72**, 4B9 (1991).
14. A. A. Pavlov, M. J. Mills, O. B. Toon, *Geophys. Res. Lett.* **32**, 10.1029/2005GL0227B4 (2005).
15. Materials and methods are available as supporting material on *Science* Online.
16. M. R. Legrand, R. J. Delmas, *Atmas. Environ.* **18**, 1B67 (19B4).
17. J. Cole-Dai, E. Mosley-Thompson, *Ann. Glacial.* **29**, 99 (1999).
1B. M. Legrand, D. Wagenbach, *J. Geophys. Res.* **104**, 15B1 (1999).
19. N. Patris, R. J. Delmas, J. Jouzel, *J. Geophys. Res.* **105**, 7071 (2000).
20. A. W. Castleman Jr., H. R. Munkelwitz, B. Manowitz, *Tellus* **26**, 222 (1974).
21. F.-Y. Leung, A. J. Colussi, M. R. Hoffmann, *J. Phys. Chem. A* **105**, B073 (2001).
22. J. B. Burkholder, S. McKeen, *Geophys. Res. Lett.* **24**, 3201 (1997).
23. S. Ono *et al.*, *Earth Planet. Sci. Lett.* **213**, 15 (2003).
24. S. J. Mojzsis, C. D. Coath, J. P. Greenwood, K. D. McKeegan, T. M. Harrison, *Geochim. Casmachim. Acta* **67**, 1635 (2003).
25. K. Chung, J. G. Calvert, J. W. Bottenheim, *Int. J. Chem. Kinet.* **7**, 161 (1975).
26. E. Castellano *et al.*, *J. Geophys. Res.* **110**, 10.1029/2004JD005259 (2005).
27. We acknowledge useful discussions with S. Bekki and thank the Conseil Régional Rhônes-Alpes for partially supporting travel expenses for M.B. J.S. acknowledges the Balzan Foundation for financial support; C. Lorius and the Institut National des Sciences de l'Univers (INSU) for mass spectrometry acquisition; the French Polar Institute and M. Legrand (Institut Polaire Francais Paul Emile Victor program DC17) for logistical support in Antarctica; the CNRS, under its Programme International de Coopération Scientifique; and the INSU Programme National de Chimie Atmosphérique. The NSF Office of Polar Programs provided financial support for M.H.T. We also thank J. McCabe and U. Morgenstern for helping J.S. to dig the snow pit.

CO₂-Forced Climate and Vegetation Instability During Late Paleozoic Deglaciation

Isabel P. Montañez,[1]* Neil J. Tabor,[2] Deb Niemeier,[3] William A. DiMichele,[4] Tracy D. Frank,[5] Christopher R. Fielding,[5] John L. Isbell,[6] Lauren P. Birgenheier,[5] Michael C. Rygel[5]†

The late Paleozoic deglaciation is the vegetated Earth's only recorded icehouse-to-greenhouse transition, yet the climate dynamics remain enigmatic. By using the stable isotopic compositions of soil-formed minerals, fossil-plant matter, and shallow-water brachiopods, we estimated atmospheric partial pressure of carbon dioxide (pCO_2) and tropical marine surface temperatures during this climate transition. Comparison to southern Gondwanan glacial records documents covariance between inferred shifts in pCO_2, temperature, and ice volume consistent with greenhouse gas forcing of climate. Major restructuring of paleotropical flora in western Euramerica occurred in step with climate and pCO_2 shifts, illustrating the biotic impact associated with past CO_2-forced turnover to a permanent ice-free world.

A decade of studying Pleistocene ice cores has unequivocally documented a strong coupling of atmospheric partial pressure of CO_2 (pCO_2) and surface temperatures with changing global ice volume (1, 2). Although the precise mechanistic link between atmospheric greenhouse gases and climate is debated, there remains little doubt that high concentrations of atmospheric CO_2 have strongly amplified Earth's past climates. Anthropogenic CO_2 emissions have increased atmospheric CO_2 to concentrations higher than at any time in at least the past 650,000 years and could increase it to more than 2000 parts per million by volume (ppmv) as accessible fossil fuel reservoirs are exhausted (3). The last time such concentrations were seen on Earth was at the onset of our modern

icehouse [$\sim$40 to 34 million years ago (Ma)], a transition from ice-free to glacial conditions characterized by repeated C cycle perturba-

[1]Department of Geology, University of California, Davis, CA 9S616, USA. [2]Department of Geological Sciences, Southern Methodist University, Dallas, TX 7527S, USA. [3]Department of Civil and Environmental Engineering, University of California, Davis, CA 9S616, USA. [4]Department of Paleobiology, Smithsonian Museum of Natural History, Washington, DC 20S60, USA. [5]Department of Geosciences, 214 Bessey Hall, University of Nebraska, Lincoln, NE 68S88, USA. [6]Department of Geosciences, University of Wisconsin, Post Office Box 413, Milwaukee, WI 53201, USA.

*To whom correspondence should be addressed. E-mail: montanez@geology.ucdavis.edu
†Present address: Department of Geology, State University of New York, College at Potsdam, Potsdam, NY 13676, USA.

tion, large magnitude changes in atmospheric pCO_2, and major ephemeral warmings (*4*, *5*). As our climate system departs from the well-studied Pleistocene glacial-interglacial cycles, a deep-time perspective of pCO_2-climate-glaciation linkages is essential for a fuller understanding of what may be the Earth's most epic deglaciation.

We present here the results of a multipronged investigation that provides evidence for significantly changing atmospheric CO_2 concentrations and surface temperatures during a 40-million-year period of the late Paleozoic (~305 to 265 Ma), which encompasses the deterioration of the most widespread and long-lived icehouse of the last half-billion years (*6*). This global warming event accompanied a permanent transition to an ice-free world, a condition that arguably lasted until the current glacial state. These results, when integrated with a newly emerging glaciation history for southern Gondwana (*7–11*), indicate strong linkages between pCO_2, climate, and ice-mass dynamics during the final stages of the Late Paleozoic Ice Age (end of LPIA). Integration of these climate proxy records with our newly developed tropical paleobotanical records shows repeated climate-driven ecosystem restructuring in western paleoequatorial Euramerica.

The CO_2 contents of ancient atmospheres can be estimated from the carbon stable isotope values ($\delta^{13}C$) of ancient soil-formed carbonates and goethites with an uncertainty of $\leq\pm500$ ppmv (*12*, *13*). These minerals are the proxy of choice when pCO_2 is high (≥1000 ppmv), whereas the method's sensitivity decreases at lower pCO_2 (<800 ppmv) (*14*, *15*). The precision of pCO_2 estimates reflects the variable assumptions used for each pCO_2 calculation (*16*), which can be further refined if the $\delta^{13}C$ of coexisting organic matter is available and if quantitative estimates of paleosoil-respired CO_2 content and paleotemperatures can be inferred from modern analogs or independently derived geochemical proxies (*15*).

To reconstruct atmospheric CO_2 during the end of the LPIA, we measured the $\delta^{13}C$ values of soil-formed calcites ($\delta^{13}C_{carb}$) collected from mature, well-drained profiles from the Eastern Shelf of the Midland Basin; the Pedregosa, Anadarko, and Paradox Basins; and the Grand Canyon Embayment of western paleoequatorial Euramerica (fig. S1 and table S1) (*17*). We consider measured paleosol $\delta^{13}C_{carb}$ values to be a robust proxy of soil-water CO_2 during formation, given the lack of evidence for mineral recrystallization and overgrowth and their overall shallow and low-temperature burial histories (*18*). Furthermore, we consider the $\delta^{13}C$ of well-preserved fossil plant matter ($\delta^{13}C_{org}$) to be a faithful proxy of the C isotope composition of soil-respired CO_2 and, in turn, of atmospheric CO_2 (*19*, *20*). Compression and permineralized fossil plants, cuticles, coal, and charcoal were collected from mudstone deposits of abandoned
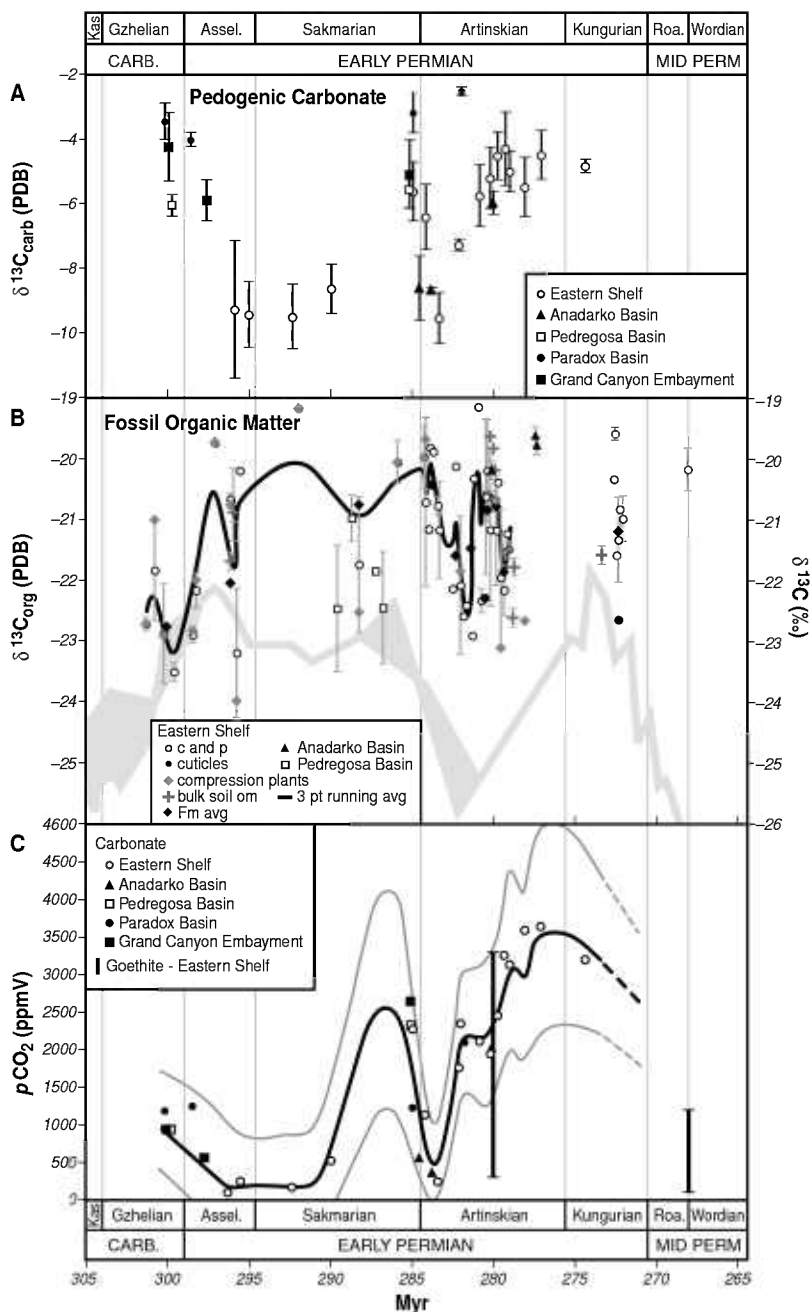

Fig. 1. Temporal distribution of carbonate (**A**) and fossil plant (**B**) $\delta^{13}C$ values used to construct best estimate of Permo-Carboniferous atmospheric pCO_2 (**C**). Individual points in (A) and (B) are the average of analyses from suites of contemporaneous paleosols (from 5 to 18) and associated plant localities (from 3 to 21); "c and p" encompasses all compression and permineralized plant matter, coals, and charcoals. Vertical bars are ±2 SE around the mean. PDB, Pee Dee belemnite. (B) Solid curve is three-point weighted running average through samples from the Eastern Shelf, Midland Basin. Gray band is $\delta^{13}C_{org}$ of Permo-Carboniferous coals from three correlated successions in North China Platform (*22*). Overlapping $\delta^{13}C_{org}$ trends but different $\delta^{13}C_{org}$ values are interpreted to reflect overall wetter conditions for the North China Platform relative to western paleoequatorial Euramerica in the Permian. Data and pCO_2 presented on an age model (*51*) developed for the terrestrial composite section by linearly interpolating between known biostratigraphic boundaries. (C) Best estimate of paleo-pCO_2 (black curve) from Monte Carlo simulation of chronostratigraphically well-constrained sample populations; uncertainty in pCO_2 estimates (gray curves) reflects variability in $\delta^{13}C_{carb}$ and $\delta^{13}C_{org}$, interpreted to record inter- and intrabasinal variations in soil conditions, vegetation, and climate. Vertical bars are published goethite-based CO_2 estimates from the same set of paleosols (*25*).

fluvial channels and floodplains, which are stratigraphically intercalated (on a sub-10-m resolution) with carbonate-bearing paleosols (table S2). The use of measured $\delta^{13}C_{org}$ rather than penecontemporaneous marine carbonates as a proxy of atmospheric $\delta^{13}C$ reflects a growing appreciation of local-scale C cycling effects on the $\delta^{13}C$ values of epicontinental marine carbonates (21). The terrestrial $\delta^{13}C_{carb}$ and $\delta^{13}C_{org}$ time series have an average sampling interval of <1 million years (My) and define long-term trends that exhibit systematic variability (Fig. 1, A and B). That the long-term $\delta^{13}C_{org}$ trend records first-order variations in atmospheric $\delta^{13}C$ is supported by its similarity to time-equivalent $\delta^{13}C_{org}$ records of Permo-Carboniferous

coals from the North China Platform (22) and by a narrow range, throughout the study area, in the ratio of intracellular, pi, and atmospheric, pa, partial pressures of CO_2 in paleoflora [0.46 to 0.57 ± 0.3 (2 SE)], which were estimated by using measured $\delta^{13}C_{org}$ values of fossil plants and $\delta^{13}C_{carb}$ values of contemporaneous marine brachiopods (17). These factors indicate that changes in geomorphic or environmental conditions in the study area were secondary to atmospheric $\delta^{13}C$ in influencing measured fossil-plant $\delta^{13}C_{org}$ values.

Ranges of paleosoil-respired CO_2 content were inferred from the morphologies of suites of contemporaneous paleosols (23) by comparison with modern analogs, addressing a major source

of uncertainty in previous applications of the CO_2 paleobarometer (table S3) (14, 15). Paleosol temperatures were inferred from the oxygen and hydrogen isotopic compositions of pedogenic phyllosilicates and Fe oxides obtained from the same set of paleosols (18, 24). The best estimate of paleoatmospheric pCO_2 was defined by using Monte Carlo simulation involving 1000 randomly drawn samples for each variable for each time-location combination (17). Monte Carlo simulation uses random sampling techniques to stochastically solve physical process problems, in this case quantitatively estimating paleo-pCO_2 and the associated uncertainty by integrating across all of the inferred and measured input variables.

Modeled CO_2 concentrations (Fig. 1C and table S4) define a long-term rise from an average of present atmospheric levels (PAL = 280 ppmv) in the earliest Permian to values of up to 3500 ppmv by the late Early Permian. A substantial decline in pCO_2 into the early Middle Permian is corroborated by independently derived goethite-based estimates of Permian pCO_2 (25). A short-lived (~2 My) drop in pCO_2 to near PAL, defined by contemporaneous paleosols, punctuates the Early Permian rise. Modeled pCO_2 suggests that PAL values were limited to the earliest Permian after latest Carboniferous levels of up to 1000 ppmv, in accord with pCO_2 inferred from marine carbonate $\delta^{13}C$ (26) and with southern Gondwanan sedimentologic and geochemical evidence for latest Carboniferous warming (9, 27). Our record refines the structure of well-established pCO_2 reconstructions, which indicate sustained PAL values throughout much of the Permo-Carboniferous (15, 28, 29). The higher-frequency oscillations revealed by this study would be below the temporal resolution (5 to 20 My time-averaging) of those long-term CO_2 records.

In order to evaluate the nature of the CO_2-climate relationship, we developed a time-equivalent record of paleotropical sea-surface temperatures (SSTs) by using $\delta^{18}O$ values from a global compilation of well-preserved latest Carboniferous through Middle Permian tropical shallow-water brachiopods (table S5) (30); brachiopods have diagenetically resistant, low-Mg calcitic shells that incorporate oxygen isotopes in equilibrium with seawater (31). The residual brachiopod $\delta^{18}O$ record (Fig. 2A) displays clear isotopic fluctuations, with intervals of maximum values corresponding to Permian glacial maxima or marked coolings in Antarctica and/or Australia (10, 11) and, to the degree afforded by geochronologic dates, with the younger periods of inferred glacial maxima in the Karoo Basin (8, 32), southern Argentina (9), and Tasmania (33). Intervals of minimum $\delta^{18}O_{carb}$ values correspond with independently inferred periods of marked warming and sea-level rise (7–9, 34) (Fig. 2C).

Inferring secular paleotemperatures from $\delta^{18}O_{carb}$ requires careful consideration of the compound effects on values of continental ice
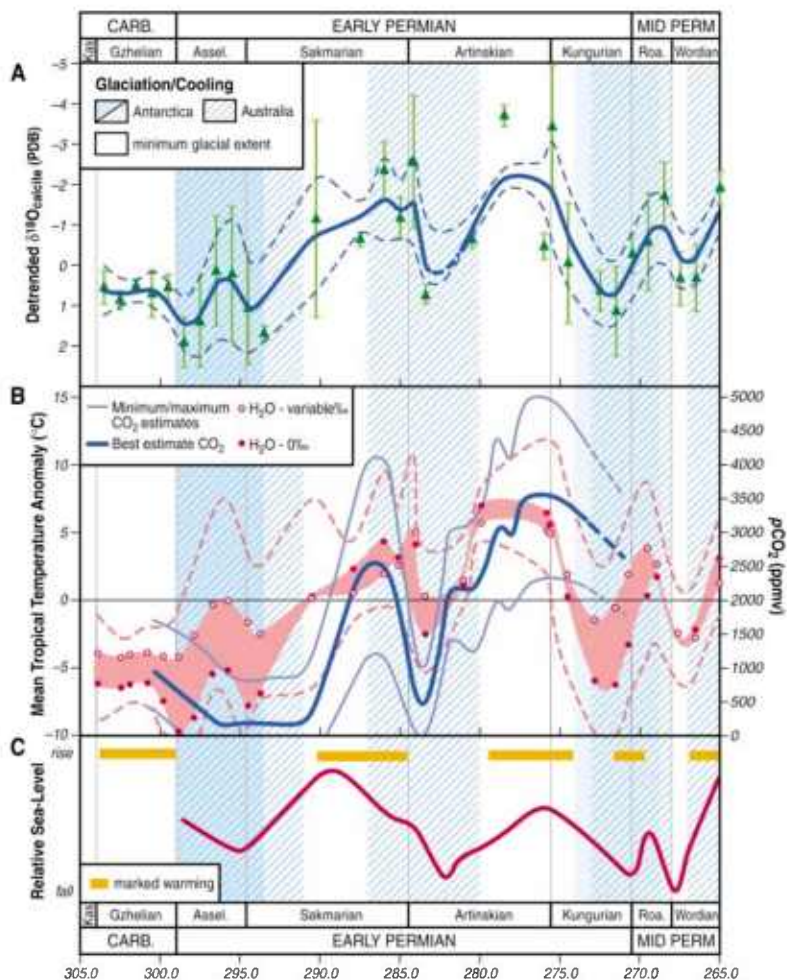

Fig. 2. Relationship among Permo-Carboniferous pCO_2, climate, and cryosphere. Temporal distribution of glacial maxima and/or cool periods based on stratigraphic distribution of diamictites, rhythmites, and dropstone and keel turbate structures in Antarctica and Australian glacigenic deposits (10, 11). (**A**) Three-point weighted running average (blue curve) and ±2 SE (dashed curves) of detrended $\delta^{18}O_{brachiopod}$ values binned into 1- to 3-My windows (green triangles). Error bars indicate ±2 SE around the mean $\delta^{18}O_{brachiopod}$ values. (**B**) Inferred paleotropical SSTs (red interval) (40) are reported as temperature anomalies given the potential effects of local and regional environmental and diagenetic influences on brachiopod $\delta^{18}O$. Paleo-SST anomalies (relative to 17.5° C) were calculated from a three-point weighted running average (± 2 SE) through $\delta^{18}O$-based paleotemperature estimates (table S5). Blue curves are best estimate (heavy) and uncertainty (light) of paleo-pCO_2. (**C**) Relative sea-level curve compiled from (8, 53); distribution of warm intervals, from (7–9) and (34).

volume, local hydrography, and SST, as well as any vital effects and postdepositional alteration (*31, 35*). The eustatic component in the Permo-Carboniferous brachiopod $\delta^{18}O$ record due to ice volume variability likely accounts for far less than 2 per mil (‰) of the observed $\delta^{18}O$ variation given reconstructed amplitudes (10 to <100 m) of Permo-Carboniferous glacio-eustasy (*10*) and an O isotope composition of seawater ($\delta^{18}O_{sw}$)–sea level relationship of 0.1‰ per 10 m of sea level change (*36*). The residual secular $\delta^{18}O_{carb}$ signal is interpreted to record changes in temperature, salinity, and

pH. Local hydrographic variations in tropical epicontinental seas would have dampened the magnitude of $\delta^{18}O_{carb}$ shifts, given hypothesized heightened freshwater discharge to continental shelves (decreased salinity and lowered $\delta^{18}O_{sw}$) during late Paleozoic periods of maximum glaciation, and increased evaporation (increased salinity and $\delta^{18}O_{sw}$) during drier, highly seasonal glacial minima (*36*). Moreover, paleo-SSTs under elevated pCO_2 may be underestimated by up to 2°C, given that lowered seawater pH would have shifted $\delta^{18}O_{carb}$ to less negative values (*38, 39*).

The amplitudes of the reconstructed SST shifts (*40*) indicate substantial changes in the mean state of tropical climate during the end of the LPIA, with glacial tropical oceans at least 4° to 7°C cooler than those of intervening glacial minima (Fig. 2B). Inferred periods of elevated tropical SSTs and pCO_2 coincide with independently recognized intervals of warmer temperate conditions in high-latitude southern Gondwana (Fig. 2C) indicated by the accumulation of nonglacial sediments, including extensive kaolin and bauxite deposits in Australia during peak (Artinskian) warming and pCO_2 (*7*) and increased faunal diversity in Australia and South America (*7, 11, 41*). The covariance among inferred shifts in paleotropical SSTs, pCO_2, and variations in high-latitude Gondwanan glaciation and climate implies a strong CO_2-climate-glaciation linkage during the Permian. Although our coupled records suggest atmospheric CO_2 may have played a direct role in forcing Early to Middle Permian climate and ice mass stability, a determination of phase relationships between these parameters is precluded by the uncertainties in the age models. The inferred variations in tropical SSTs between periods of glacial maxima and minima, however, are consistent with the range predicted by Permian climate simulations for a change in radiative CO_2 forcing from 1 to 8 PAL (*42*).

Permo-Carboniferous plant assemblages from western paleoequatorial Euramerica archive a mechanistic vegetational response to late Paleozoic pCO_2 and climate change. Reconstructed plant communities from the same terrestrial successions that host the pedogenic mineral-bearing paleosols document major dominance-diversity changes corresponding one-for-one to inferred changes in paleotropical climate, pCO_2, and glacial extent (Fig. 3 and table S6). Four tropical biomes appear in succession, composed of increasingly xeromorphic species, representing progressively more seasonally moisture-stressed environments. These biomes are floristically distinct, sharing only a few opportunistic ferns and sphenopsids (*43*). Typical latest Carboniferous flora, rich in marattialean ferns, medullosan pteridosperms, sphenopsids, and sigillarian lycopsids, was replaced essentially instantaneously by one rich in conifers {*Walchia* and *Ernestiodendron*; compare with *Brachyphyllum* (*44*), callipterids (*Rhachiphyllum*), cycadophytes (*Russellites*), and other seed plants [*Cordaites*, *Sphenopteridium* (*45*)]}. This floristic shift is synchronous with an abrupt continental climate transition from everwet to semi-arid conditions (Fig. 3A), characterized by increased temperatures (*18, 24*) and seasonal moisture availability inferred from paleosol morphologies (*23*).

Conifers and callipterids diversified in seasonally dry habitats during the initial Early Permian (Sakmarian) rise in CO_2 and the warm period of glacial minima, spatially replacing the tree fern–rich and the pteridosperm-rich wetland floras (Fig. 3). Tree fern–rich floras reappeared during wetter, cooler conditions of the mid-Early
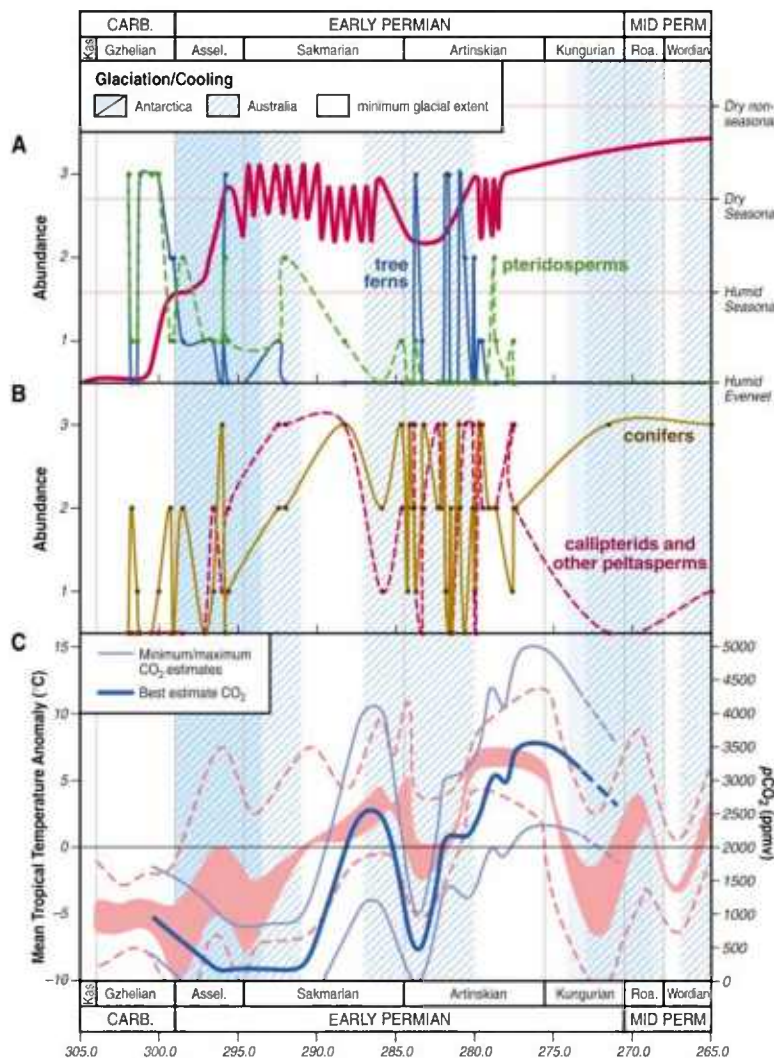

Fig. 3. Patterns of abundance change in major flora of study area (**A** and **B**) and comparison to independently derived Permo-Carboniferous climate and pCO_2 (**C**). Plants from 49 sampling localities on the Eastern Shelf, Midland Basin, are rank ordered: 1, rare (occurs in <10% of sampling quadrats at any given locality), 2, common (occurs in 10 to 50% of sampling quadrats), and 3, abundant (occurs in >50% of sampling quadrats). (A) Tree ferns and pteridosperms are hygromorphic and occur in deposits with sedimentologic and pedogenic indicators of everwet to subhumid seasonal conditions. Red climate curve for paleoequatorial western Euramerica defined by using soil moisture regimes and degree of seasonality inferred from paleosol morphologies (*23*); zigzag pattern indicates short-term (10^3 to 10^5 year) climate cycles inferred from intervals of polygenetic soils that exhibit climatically out-of-phase superposition of calcic and argillic horizons. (B) Conifers and peltasperms are xeromorphic and typically are found in association with sedimentologic and pedogenic indicators of moisture limitation.

Permian (Artinskian) glaciation, stratigraphically intercalated but not mixed, with conifer-callipterid floras. These two glacial floras show limited species overlap and oscillated at the 10^3- to 10^5-year scale, reflecting short-lived pluvials (*46*). Dramatic floristic changes also occurred during the cold period at the close of the Early Permian (Kungurian), with the migration into lowland basins of unique seed-plant assemblages not observed again until the Late Permian (conifers) and the Mesozoic (cycads) (*47*). These temporally successive floras tracked climatic conditions and contained progressively more evolutionarily advanced lineages. This suggests that evolutionary innovation, the appearance of new plant body plans, occurred in extrabasinal areas and was revealed by climate-driven floral migration into lowland basins.

The history of latest Carboniferous to Middle Permian climate provides a unique deep-time perspective on the precarious balance between icehouse and greenhouse states during major climate transitions, which are coupled to changing atmospheric CO_2 content. Maximum expansion of Gondwanan continental ice sheets occurred during earliest Permian time (*10*) under the lowest paleoatmospheric CO_2 levels and paleotropical SSTs. Widespread Early Permian (mid-Sakmarian) collapse of ice sheets (*8, 10*) coincided with the onset of rising atmospheric CO_2 levels, after which time tropical SSTs and pCO_2 rose. Subsequent glacial influence was restricted to eastern Australia (*6*), with resurgent ice masses occurring during three more episodes (*11*) of lowered atmospheric pCO_2 before the permanent transition to an ice-free world (260 Ma). Our study indicates that ice buildup in Australia during subsequent cold periods, however, was progressively less widespread, with the two youngest glacials generally confined to local valleys or mountain ice caps along the polar margin of Australian Gondwana. Notably, SSTs and pCO_2 did not return to earliest Permian levels during these post-Sakmarian glacial periods.

Our reconstructed pCO_2, paleotemperatures, and inferred glacial history depict an Early Permian atmosphere that systematically increased from PAL to levels similar to those predicted to exist if fossil fuels are exhausted. Although global-scale deglaciation was unrelenting under rising Early Permian atmospheric CO_2, transient periods of icehouse stability and glacial resurgence returned during short-lived intervals of low pCO_2, perhaps until a CO_2 threshold and greenhouse stability precluded the reestablishment of glacial conditions [compare with (*48*)]. This late Paleozoic climate behavior mimics, in reverse, the magnitude and temporal scale of atmospheric CO_2 changes and ephemeral warmings that foreshadowed the transition into our present glacial state (*4, 5*), further documenting the degree of climate variability, carbon cycle perturbation, and tropical ecosystem restructuring that has been associated with past CO_2-forced climate transitions.

References and Notes

1. J. R. Petit *et al.*, *Nature* **399**, 429 (1999).
2. U. Siegenthaler *et al.*, *Science* **310**, 1313 (2005).
3. L. R. Kump, *Nature* **419**, 188 (2002).
4. M. Pagani, J. C. Zachos, K. H. Freeman, B. Tipple, S. Bohaty, *Science* **309**, 600 (2005); published online 16 June 2005 (10.1126/science.1110063).
5. A. Tripati, J. Backman, H. Elderfield, P. Ferretti, *Nature* **436**, 341 (2005).
6. L. A. Frakes, J. E. Francis, J. I. Syktus, *Climate Modes of the Phanerozoic* (Cambridge Univ. Press, Cambridge, 1992).
7. J. M. Dickins, *Palaeogeogr. Palaeoclimatol. Palaeoecol.* **125**, 185 (1996).
8. H. Stollhofen, I. G. Stanistreet, B. Bangert, H. Grill, *Palaeogeogr. Palaeoclimatol. Palaeoecol.* **161**, 127 (2000).
9. C. R. Gonzalez, *Palaeogeogr. Palaeoclimatol. Palaeoecol.* **79**, 275 (1990).
10. J. L. Isbell, M. F. Miller, K. L. Wolfe, P. A. Lenaker, *Geol. Soc. Am. Spec. Pap. 370* (2003), pp. 5–24.
11. A. T. Jones, C. R. Fielding, *Geology* **32**, 153 (2004).
12. T. E. Cerling, in *Palaeoweathering, Palaeosurfaces, and Related Continental Deposits*, M. Thiry, R. Simon-Coinçon, Eds. (Blackwell, Cambridge, 1999), pp. 43–60.
13. C. J. Yapp, H. Poths, *Nature* **355**, 342 (1992).
14. D. L. Royer, R. A. Berner, D. J. Beerling, *Earth Sci. Rev.* **54**, 349 (2001).
15. D. D. Ekart, T. E. Cerling, I. P. Montañez, N. J. Tabor, D. J. Beerling, *Am. J. Sci.* **299**, 805 (1999).
16. CO_2 paleobarometer input parameters include, from most to least sensitive: (i) soil-respired CO_2 content (S_z in ppmv), typically assumed to be constant, (ii) the C isotopic composition of soil-respired ($\delta^{13}C_\varnothing$) and atmospheric ($\delta^{13}C_A$) CO_2, both typically derived from broadly contemporaneous marine carbonates, and (iii) temperature, typically held constant (~25°C). Pedogenic carbonate $\delta^{13}C$ is utilized as the proxy of $\delta^{13}C$ of total soil-CO_2. For goethite-based pCO_2 estimates, the measured concentration and $\delta^{13}C$ of the Fe(CO$_3$)OH component in pedogenic goethite are taken as proxies of ambient pCO_2 and $\delta^{13}C$, respectively, present during crystallization; $\delta^{13}C_\varnothing$ and $\delta^{13}C_A$ are inferred from marine carbonate proxies or fossil organic matter.
17. Materials and methods are available as supporting material on *Science* Online.
18. N. J. Tabor, I. P. Montañez, *Palaeogeogr. Palaeoclimatol. Palaeoecol.* **223**, 127 (2005).
19. The $\delta^{13}C_{org}$ values of matrix in calcic-paleosols and contemporaneous fossil-plant matter overlap (Fig. 1B), indicating that the latter are representative of soil-respired CO_2 in carbonate-bearing paleosols. A $\delta^{13}C_{atm}$ proxy record was calculated assuming isotopic equilibrium fractionation (Δ_{atm-om} of 18.5‰) between paleoflora ($\delta^{13}C_{org}$) and atmospheric CO_2. Paleo-pCO_2 estimated using a 2‰ variation in Δ_{atm-om} falls within the uncertainty band shown on Fig. 1C, reflecting the low sensitivity of the model to $\delta^{13}C_A$.
20. N. C. Arens, A. H. Jahren, R. Amundson, *Paleobiology* **26**, 137 (2000).
21. K. M. Panchuk, C. Holmden, S. A. Leslie, *J. Sediment. Res.* **76**, 200 (2006).
22. H. Zhang, G. Shen, Z. He, *Acta Geol. Sin.* **73**, 111 (1999).
23. N. J. Tabor, I. P. Montañez, *Sedimentology* **51**, 851 (2004).
24. N. J. Tabor, *Earth Planet. Sci. Lett.*, in press.
25. N. J. Tabor, C. J. Yapp, I. P. Montañez, *Geochim. Cosmochim. Acta* **68**, 1503 (2004).
26. M. R. Saltzman, *Geology* **31**, 151 (2003).
27. K. Scheffler, S. Hoernes, L. Schwark, *Geology* **31**, 605 (2003).
28. R. A. Berner, Z. Kothavala, *Am. J. Sci.* **301**, 182 (2001).
29. C. I. Mora, S. G. Driese, L. A. Colarusso, *Science* **271**, 1105 (1996).
30. Published $\delta^{18}O$ data are from biostratigraphically constrained and diagenetically screened calcitic brachiopods (*31, 35, 49*); $\delta^{18}O$ values < −8‰ were excluded. The $\delta^{18}O$ values were detrended to remove the effects of the long-term linear Phanerozoic trend by removing, from each data point, the least squares linear fit calculated using SPlus.
31. H. Mii, E. Grossman, T. E. Yancey, *Geol. Soc. Am. Bull.* **111**, 960 (1999).
32. B. Bangert, R. Armstrong, H. Stollhofen, V. Lorenz, *J. Afr. Earth Sci.* **29**, 33 (1999).
33. M. R. Banks, in *Earth's Pre-Pleistocene Glacial Records*, M. J. Hambrey, W. B. Harland, Eds. (Cambridge Univ. Press, Cambridge, 1981), pp. 495–501.
34. J. N. J. Visser, *Sedimentology* **44**, 507 (1997).
35. C. Korte, T. Jasper, H. W. Kozur, J. Veizer, *Palaeogeogr. Palaeoclimatol. Palaeoecol.* **224**, 333 (2005).
36. D. P. Schrag *et al.*, *Quat. Sci. Rev.* **21**, 331 (2002).
37. C. B. Cecil *et al.*, in *Climate Controls on Stratigraphy*, C. B. Cecil, T. N. Edgar, Eds. (SEPM Special Publication 77, Society for Sedimentary Geology, Tulsa, OK, 2003), pp. 151–180.
38. D. L. Royer, R. A. Berner, I. P. Montañez, N. J. Tabor, D. J. Beerling, *Geol. Soc. Am. Today* **14**, 3 (2004).
39. W. C. Beck, E. L. Grossman, J. W. Morse, *Geochim. Cosmochim. Acta* **69**, 3493 (2005).
40. Detrended $\delta^{18}O$ values were binned into 1- to 3-My windows. Average values (±2 SE) were translated to a range of paleotropical SSTs by using a quadratic equation (*50*) and a constant (0‰) or variable (−0.5 to +1.5‰) $\delta^{18}O_{sw}$. The influence of local and environmental factors and diagenesis on the long-term $\delta^{18}O_{carb}$ trend is considered secondary, given the overlap in individual published datasets and Tethyan and Panthalassan brachiopod $\delta^{18}O$ values; secondary influences are likely recorded in the $\delta^{18}O_{brachiopod}$ variability within contemporaneous populations.
41. O. R. Lopez-Gamundi, in *Late Glacial and Postglacial Environmental Changes: Quaternary, Carboniferous-Permian, and Proterozoic*, I. P. Martini, Ed. (Oxford Univ. Press, Oxford, 1997), pp. 147–168.
42. A. M. E. Winguth *et al.*, *Paleoceanography* **17**, 1057 (2002).
43. W. A. DiMichele, R. B. Aronson, *Evolution* **46**, 807 (1992).
44. Compare with *Brachyphyllum* after S. H. Mamay, *U.S. Geol. Surv. Prof. Pap. 575-C* (1967), p. 120.
45. *Sphenopteridium*, after S. H. Mamay, *Am. J. Bot.* **79**, 1092 (1992).
46. W. A. DiMichele, N. J. Tabor, D. S. Chaney, W. J. Nelson, *Geol. Soc. Am. Spec. Pub. 299* (2006), pp. 223–248.
47. W. A. DiMichele, D. S. Chaney, W. H. Dixon, W. J. Nelson, R. W. Hook, *Palaios* **15**, 524 (2000).
48. L. R. Kump, *Nature* **436**, 333 (2005).
49. J. Veizer *et al.*, *Chem. Geol.* **161**, 59 (1999).
50. S. T. Kim, J. R. O'Neil, *Geochim. Cosmochim. Acta* **61**, 3461 (1997).
51. A chronostratigraphic framework for the Eastern Shelf of Texas (*23*) was used as the basis for the composite section into which other records were integrated with use of available biostratigraphy and lithostratigraphic correlation. Calibration of the Eastern Shelf succession to the Gradstein *et al.* 2004 geologic time scale (*52*) is based, for the study area, on the stratigraphic position of the stage boundaries determined by conodont, fusulinid, and ammonite biostratigraphy.
52. F. M. Gradstein, J. G. Ogg, A. G. Smith, Eds., *A Geologic Time Scale 2004* (Cambridge Univ. Press, Cambridge, 2005).
53. C. A. Ross, J. R. P. Ross, in *Sea-Level Changes: An Integrated Approach*, C. K. Wilgus *et al.*, Eds. (SEPM Special Publication 42, Society for Sedimentary Geology, Tulsa, OK, 1988), pp. 227–247.
54. We thank D. Chaney and G. Mack for field guidance and discussions; J. Fong for the illustrations; and H. Jahren, R. Berner, T. Cerling, and three anonymous reviewers for critical insight. Supported by NSF grants EAR-9914640, EAR-0417578, EAR-0545701, OPP-0126086, and ANT-0440919.